Time and Space-correlated Plasma Property Measurements in the Near-field of a Coaxial Hall Discharge

IEPC-2009-135

Presented at the 31st International Electric Propulsion Conference,
University of Michigan • Ann Arbor, Michigan • USA
September 20 – 24, 2009

Andrew W. Smith[1] and Mark A. Cappelli[2]
Stanford Plasma Physics Laboratory, Stanford University, Stanford, CA, 94305-3032, USA

Abstract: Space and time-correlated measurements of floating and plasma potential are made in the near-field of a coaxial Hall plasma discharge using an emissive probe which is synchronized to breathing mode fluctuations in discharge current. The resulting 3D maps show that the luminous, beam-like feature frequently observed emanating from the central pole of operating plasma accelerators is found to be concomitant with a spike in the plasma potential (and electron temperature). The structure of the plasma potential allows for multiple avenues for back-streaming ions to accelerate towards the discharge front pole and may pull some classes of ions toward the central axis. The fluctuations in plasma properties exhibit complex structure at frequencies on the order of the breathing mode; most notably, the plasma potential appears to fluctuate in a helical fashion, resembling tilted drift-waves rotating about the central axis. The azimuthal velocity of this fluctuation is found to be 1.8 km/s. A simple analysis of these waves draws attention to the possible role that they may play in driving anomalous cross-field electron transport in the near-field region.

Nomenclature

$\boldsymbol{B}$	=	magnetic field vector
c_i	=	ion sound speed
e	=	fundamental charge
$\boldsymbol{E}$	=	electric field vector
i	=	imaginary number
j_{em}	=	current density of emitted electrons that reach the plasma
j_e^{sat}	=	electron saturation current density
k	=	Boltzmann's constant
k_z	=	axial wave number
k_θ	=	azimuthal wave number
$k_\perp$	=	perpendicular wave number
$L_{\nabla n}$	=	characteristic scale of density gradients
m_e	=	electron mass
m_i	=	ion mass
n_e	=	electron number density
n_o	=	number density of plasma
r_m	=	mean radius of thruster channel
r_p	=	probe radius
t	=	time

[1] Graduate Research Assistant, Mechanical Engineering Department, awsmith@stanford.edu.
[2] Professor, Mechanical Engineering Department, cap@stanford.edu.

T_e = electron temperature
$\tilde{T}_e$ = electron temperature calculated assuming that ions enter the sheath at the Bohm velocity
x = x-coordinate (parallel to exit plane of thruster)
$\tilde{X}$ = x-coordinate non-dimensionalized by the mean channel radius
y = y-coordinate, with $y = 0$ defining a plane which intersects the thruster centerline and cathode exit
$\tilde{Y}$ = y-coordinate non-dimensionalized by the mean channel radius
z = axial coordinate, with $z = 0$ being the exit plane
$\tilde{Z}$ = z-coordinate non-dimensionalized by the mean channel radius
α = parameter proportional to growth rate of drift wave instability
$\Delta\phi^*$ = correction to plasma potential
λ_D = Debye length
ρ_s = ratio of ion acoustic speed to ion cyclotron frequency
ϕ_c = floating potential of emissive probe in an unheated, cold state
ϕ_h = floating potential of heated emissive probe
ϕ_{pl} = plasma potential
$\tilde{\phi}$ = plasma potential fluctuation amplitude
ν_e = electron collision frequency
ω = drift-resistive instability frequency
ω_{ce} = electron cyclotron frequency
ω_{ci} = ion cyclotron frequency
ω_e^* = characteristic drift-wave frequency
ω_s = product of ion and electron cyclotron frequencies and the inverse electron collision frequency

I. Introduction

Coaxial Hall discharges have been used as high-specific-impulse plasma accelerators for more than 40 years[1,2]. In a typical coaxial Hall plasma accelerator (Fig. 1), the discharge is sustained in imposed orthogonal magnetic and electric fields. The magnetic field magnitude is such that the plasma electrons are strongly magnetized and confined to move predominantly in closed, azimuthal $\boldsymbol{E} \times \boldsymbol{B}$ drifts, while the plasma ions (usually xenon, but sometimes krypton and argon) are sufficiently massive to be only weakly confined and move primarily in response to the resulting electric field. As a consequence of the reduced mobility of the electrons along the direction of $\boldsymbol{E}$, localized Joule heating efficiently produces ions that are accelerated to velocities in excess of 10 km/s (e.g. Ref. 3), depending on the discharge potential established between an external cathode and an anode, often positioned at the base of the annular channel.

Within the annular wall-confined channel itself, early studies discovered the existence of axial current greater than that predicted by classical transport[4]. This "anomalous" cross-field transport of electrons has been the subject of much subsequent research. Leading candidates for the source of this anomalous transport are fluctuations in the plasma properties[4-6], often modeled using a Bohm conductivity[7], and near-wall conductivity resulting from the interaction of electrons with the channel wall[8,9]. In the near-field of Hall plasma accelerators, defined to lie between the exit of the annular channel and the external cathode, only the front-pole of the thruster serves as a confining wall, and a Bohm-model for the electron mobility is often assumed when simulating this region[10,11]. However, no clear evidence exists which links transport to plasma fluctuations in this region.

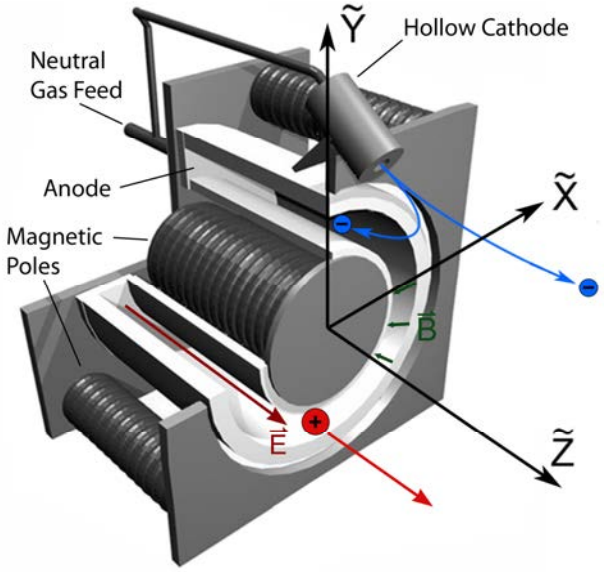

Figure 1. Schematic of a typical coaxial Hall thruster.

Understanding plasma transport within the near-

field necessitates knowledge of the electric and magnetic field structure in this region. Researchers have conducted numerous experiments to measure the time-averaged electric potential in the near-field[10,12-16], and time-correlated electron temperature and plasma potential measurements have been recorded at a discrete spatial location[17]. In this paper, we carry out similar investigations but expand them to include time- and space-correlated measurements of the floating potential, plasma potential, and electron temperature throughout much of the near-field, allowing an unprecedented visualization of the field dynamics[18]. We examine the mean (time-averaged) and low-frequency structure of these properties within the near-field of a Hall plasma accelerator that operates at relatively low power[19]. The results of our comprehensive set of emissive probe measurements show that these properties fluctuate significantly (in particular the plasma potential and electron temperature), revealing the presence of an azimuthal drift wave that may be coupled or strongly interacting with the so-called breathing mode ionization instability that is characteristic of these types of discharges[20,21]. As described below, this complex time-dependent structure may impact electron transport properties, possibly accounting for the current flow in this region.

II. Experiments

The coaxial Hall plasma accelerator studied here is a variation of a low power (nominally 200 W) discharge of the type described in the prior literature[19]. It has a co-axial channel of approximately 20 mm in length, 8 mm in width, and a mean channel radius, r_m = 11.7 mm. In this study, the discharge was operated in voltage-limited mode with a voltage and current of 200 V and 800 mA, respectively. The magnetic field peaks near the exit plane at a value of about 0.05 T, and is primarily radial at this location. The cathode keeper was maintained at 14 V and 500 mA, respectively, with 3 A of current through the heater. Argon was used as the cathode gas, with a flow rate of 2 sccm, and xenon was used as the primary discharge gas with a flow of 8.5 sccm through the channel.

The time-dependent discharge current is measured by monitoring the voltage across a shunt resistor (1.0 Ohm) at the anode side of the circuit using a differential voltage probe. Strong, periodic fluctuations in the anode current are seen due to the breathing mode ionization instability which creates macroscopic fluctuations in plasma properties within the discharge and near-field[21]. The discharge is operated in a vacuum facility consisting of a stainless-steel chamber 1.25 m in diameter and 4 m long. The base pressure in the facility during thruster operation is 1.2×10^{-5} Torr.

The potential distribution throughout the near-field of the discharge was measured using a floating emissive probe similar to that described by Haas, et al[22]. An excellent overview of plasma diagnostics, including emissive probes, is presented by Hershkowitz[23]. The emitting portion of the probe consists of a 2 mm diameter loop of 150 μm diameter thoriated-tungsten (1%) wire. The loop is oriented so that the normal to the plane formed by the loop is parallel to the *x*-direction shown in Fig. 1. The ends of this filament are mechanically crimped to copper wire and inserted into parallel holes in a 2.5 mm diameter alumina tube (generally two 26 AWG wires are utilized in each side of the alumina tube). The ends of the alumina tube are then sealed with an alumina paste. The photograph of the probe in Fig. 2 has the filament partially withdrawn from the alumina insulator, and the insulating paste has not yet been applied. Alternating current (ac) is driven through the probe and coupled through an isolation transformer so that its floating potential can be recorded on a digital oscilloscope. While other researchers have experienced problems with melting of the copper wires[24], we have found that our construction allows for probe lifetimes on the order of 2-4 hours, and the typical failure mode is evaporative mass loss in the filament itself.

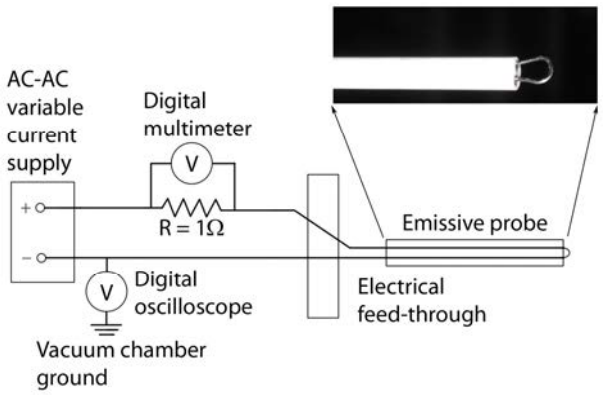

Figure 2. Schematic of the emissive probe circuit.

A detailed analysis of emissive probe characteristics is available in the literature[23,25,26], and will not be elaborated on here. A thermionic electron-emitting filament in a low-temperature plasma will float at a potential which approaches the plasma potential when the emitted electron current is sufficiently high (i.e. the filament is sufficiently heated) to neutralize the plasma sheath. Figure 3 shows a typical set of measurements of the floating potential versus applied (rms) heating current, ranging from an unheated state through probe failure. The approximate color of the filament is labeled in the figure, along with an estimate of the filament temperature[26]. As is

commonly seen in practice, the floating potential of the probe never truly saturates, but instead levels off as the heating current is increased (in the case of Fig. 3, this occurs for heating currents in excess of about 2 A). While the trace in Fig. 3 is representative of the traces obtained throughout the near field, in regions of the plasma where the probe is strongly heated by the plasma, the current needed to approach the saturated state is considerably lower. In fact, if left stationary in such regions, the probe can be made to be self-emitting even without external heating. Since there is no clear saturation of the probe, we have defined the measured plasma potential as the probe floating potential measured when it is heated with a current of 3.25 A, a value sufficiently high to be in the saturation branch at all spatial locations in the near-field studied here. While this introduces a systematic uncertainty in the extracted plasma potential (underestimating the true plasma potential by several volts), it is considered to be a reasonable trade-off as it allows us to rapidly acquire the potential by translating the probe over three-dimensional space while at a constant probe heater current. The discharge current was monitored during the tests, and the average current was found to vary by less than 1.5% for all of the points tested, regardless of the probe position relative to the thruster. In this sense, any perturbations introduced by the probe were relatively small.

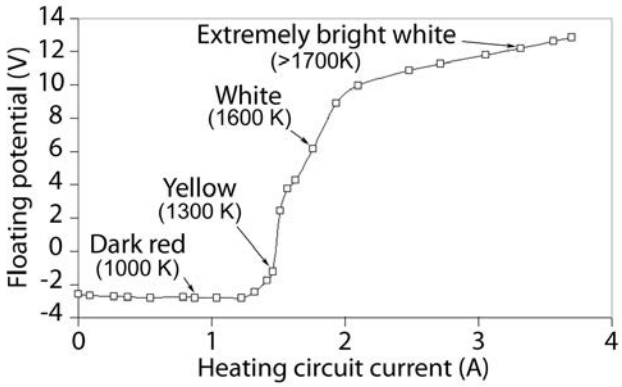

Figure 3. Floating potential versus heating current for an emissive probe (labels denote the approximate color and temperature of the filament).

The unheated (floating) potential is mapped throughout the near-field, taking care to rapidly move the probe in and out of regions of strong heating (such as very near the exit plane) so that it does not become self-emitting. Three translation stages are oriented to allow relative motion between the probe and thruster in three orthogonal directions. The thruster is mounted on a pair which allow for translational speeds of 1-3 cm/s, and the probe itself is mounted on a third stage. We use the same positioning algorithm for both the floating and plasma potential measurements, and a computer controls both the translation stages and data acquisition on a digital oscilloscope. At each measurement location, the probe is paused for one second (to allow any small residual vibrations induced by the translation stages to dampen out), after which the oscilloscope records 50,000 temporal measurements of the probe signal and discharge current simultaneously. These transient measurements are recorded at 8 ns intervals (spanning 400 μs). After the near-field floating potential measurements are complete, the probe current is raised to 3.25 A, and the measurements are repeated to obtain the plasma potential. An example trace of a typical heated probe signal and discharge current are shown in Fig. 4. The inset shows the zero-mean cross correlation of the two signals indicating a strong correlation between the probe signal and discharge current (the probe signal lags the discharge current at this point by 7.5 μs). An analysis of the power spectrum of the discharge current signal indicates a single peak between 22-29 kHz with all other frequency components having magnitudes less than 10^{-3} times that of the low-frequency peak. An analysis of the probe signal shows a single broad peak between 25 kHz and 100 kHz, with the higher end of this range having comparable frequency to transit-time instabilities[21].

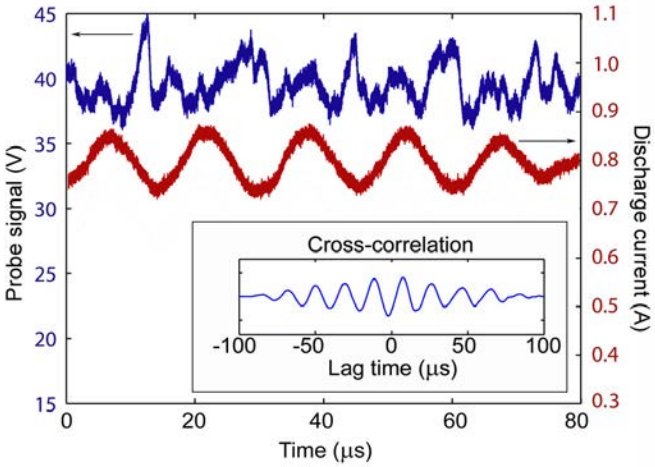

Figure 4. Representative traces of heated probe signal (blue) and discharge current (red). Inset box shows the zero-mean cross correlation of the two signals).

Determining the electron temperature, T_e, from the floating potential measured by the probe when cold and when heated requires a model of the collected electron and ion current[18,28]. In this work, we assume

$$T_e = \frac{2e(\phi_h - \phi_c)}{k \ln(m_i / 2\pi m_e)}. \quad (1)$$

Here m_i is the mass of the ions (in this case xenon), m_e is the electron mass, k is Boltzmann's constant, ϕ_h is the potential measured by the probe in the heated, emitting state, and ϕ_c is the potential measured by the probe in the unheated, cold state. The uncertainty is at least ±17%, attributable alone to the uncertainty in ion collection models[28]. In reality, the true electron temperature is expected to tend toward the higher end of the range due to the underestimation of the plasma potential.

III. Results and Analysis

Results presented here are for spatial variables nondimensionalized by the mean channel radius, r_m (i.e., $\tilde{X} = x/r_m$, $\tilde{Y} = y/r_m$, and $\tilde{Z} = z/r_m$). The coordinate convention is that shown in Fig. 1. We take $z = 0$ to be the exit plane, and $(x, y, z) = (0, 0, z)$ to define the central axis of the thruster. In all cases, the cathode body and chamber ground are assigned to 0 V. Regions where no measurements were made are indicated by filled grey or white areas. The measurements were stopped (at $z = 0.2\ r_m$) just short of the exit plane to avoid possible contact between the thruster and the probe when the translation stages were in motion. Other features of the thruster (the shape of the inner insulator, as well as the cathode location) also precluded the probing of certain regions of the near-field.

A. Time-averaged Results

The mean (time-averaged) properties calculated from the transient probe traces were interpolated to a discretization of 0.10 r_m and plotted in the left panes of Figs. 5, 6, and 7. In the $x = 0$ plane of the floating and plasma potential plots, the positions where probe measurements were obtained are indicated by open black circles, and the channel boundaries are indicated by red lines extending along z (the channel exists for $z < 0$). The channel spans a radial distance between 0.65 r_m and 1.35 r_m ($y = 0.65\ r_m$ to $1.53\ r_m$ in the $x = 0$ plane). The measurement points and channel boundaries are not shown in the other planes for clarity. The measurement locations were nearly identical in the other x-planes; however, the greatest concentration of measurements was near the center of the thruster and along the central axis where the gradients in the potential were significant.

The time-averaged floating potential (left pane of Fig. 5) shows a prominent spike along the centerline of the thruster, reaching a maximum of 18 V near $z = 1.2\ r_m$ before slowly decreasing to 7 V at $z = 5\ r_m$. This potential spike diminishes more rapidly along x and y. The floating potential near the channel exit is also elevated, although nowhere does the floating potential exceed 11 V except along the central axis. Away from the exit plane and central axis, the floating potential gradually decreases to a value between 3 and 6 V. The region of the plasma nearest to the cathode [which is located at $(x, y, z) = (0, 2.6\ r_m, 1.75\ r_m)$] is characterized by a strong depression of the floating potential, falling below -5 V. With the exception of this region near the cathode, the floating potential is considerably axisymmetric.

The magnitude of the floating potential fluctuations (i.e. the standard deviation in the floating potential temporal traces) peaks at 5 V along the central axis, near $z = 1.5\ r_m$ (see Fig. 5, right pane). The overall structure mimics the structure seen in the floating potential, although it is slightly less symmetric (with larger fluctuations present on the cathode-side of the central axis).

The plasma potential is has a much more complex structure. The time-averaged plasma potential exhibits extensive areas of elevated potential over the channel of the thruster which extend far into the near-field along the central axis (see Fig. 6). While the maximum floating potential was measured along the axis, the peak plasma potential (58 V) was measured over the channel of the thruster. The plasma potential along the central axis peaks at 45 V near $z = 2.75\ r_m$ and diminishes gradually to 35 V at $z = 4\ r_m$. The plasma potential rapidly diminishes away from the central axis, falling to < 10 V within 3-4 r_m. The central spike is narrow, with a three-dimensional beam shape. This region of elevated potential along the central axis is actually split by a narrow lower-potential valley located immediately along the central axis extending only 0.1 r_m to either side of $x, y = 0$. A depression in the plasma potential exists near the central axis for $z < \sim 1.6\ r_m$ where the potential falls to below 30 V. Surrounding this depression are regions where the plasma potential is nearly 50% higher. The upper axial boundary of this depression, which marks the transition to the elevated potential spike along the axis, corresponds with the spatial location of the onset of the drop in floating potential.

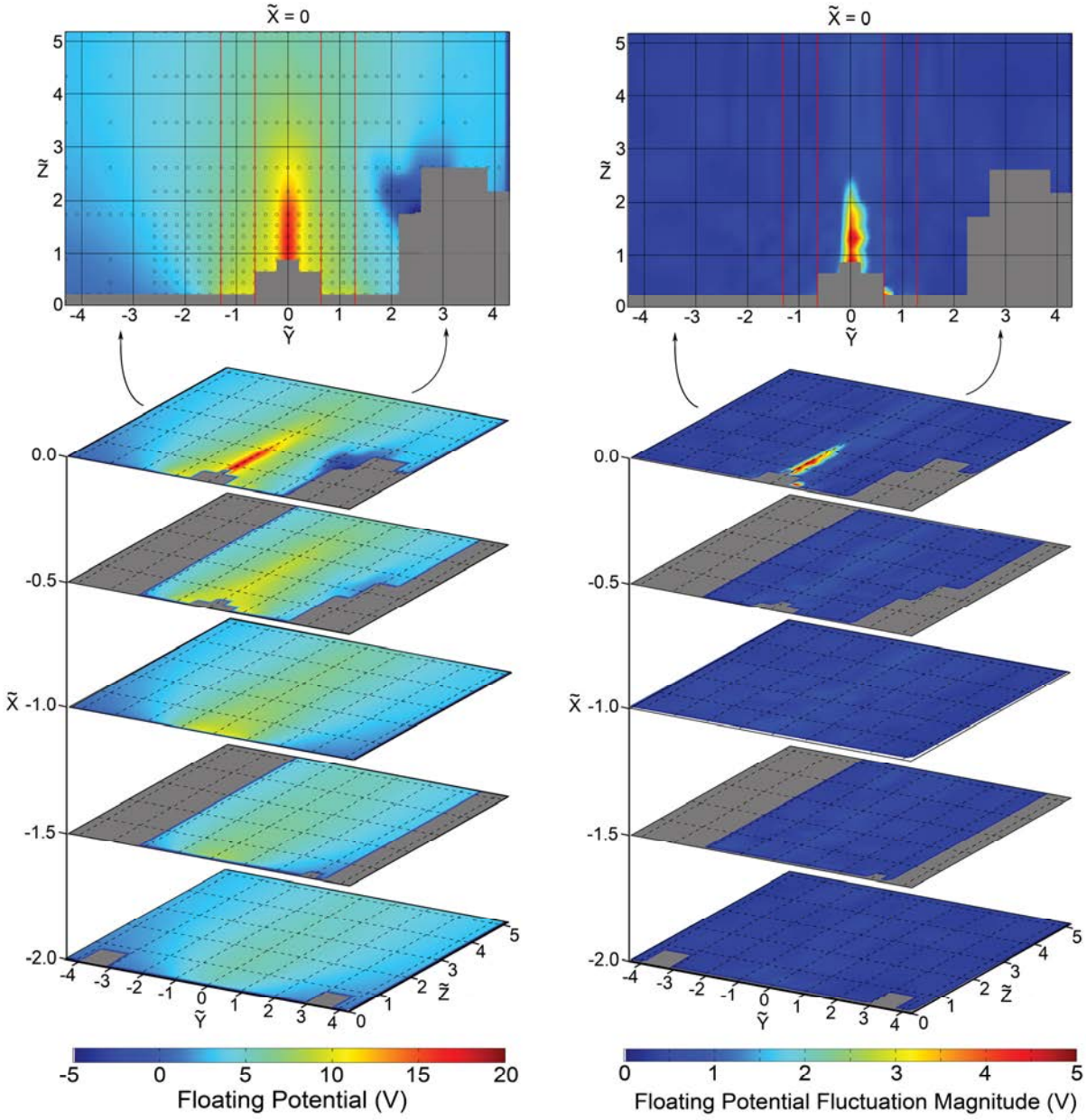

Figure 5. Spatial slices of the measured floating potential (left) and magnitude of the floating potential fluctuations (right).

The right pane of Fig. 6 shows the standard deviation of the plasma potential temporal traces. The fluctuations are most intense in the central portion of the near field of the thruster (reaching 18 V); however, they rapidly diminish for $z > 2\ r_m$. Akin to the time-averaged plasma potential, the fluctuation magnitudes also exhibit a split peak along the central axis. In general, the overall structure mimics the structure seen in the plasma floating potential, with the exception of the region along the central axis for $z < 1.6\ r_m$ where the plasma potential exhibits a depression. Here, the plasma potential fluctuations are actually quite large; in places reaching 50% of the mean value.

With the plasma and floating potential mapped out, we can determine the spatial distribution in electron temperature using Eq. (1). The resulting time-averaged electron temperature is shown in the left panel of Fig. 7. The electron temperature peaks at 10 eV directly over the channel of the thruster. Near the central axis, broad regions of

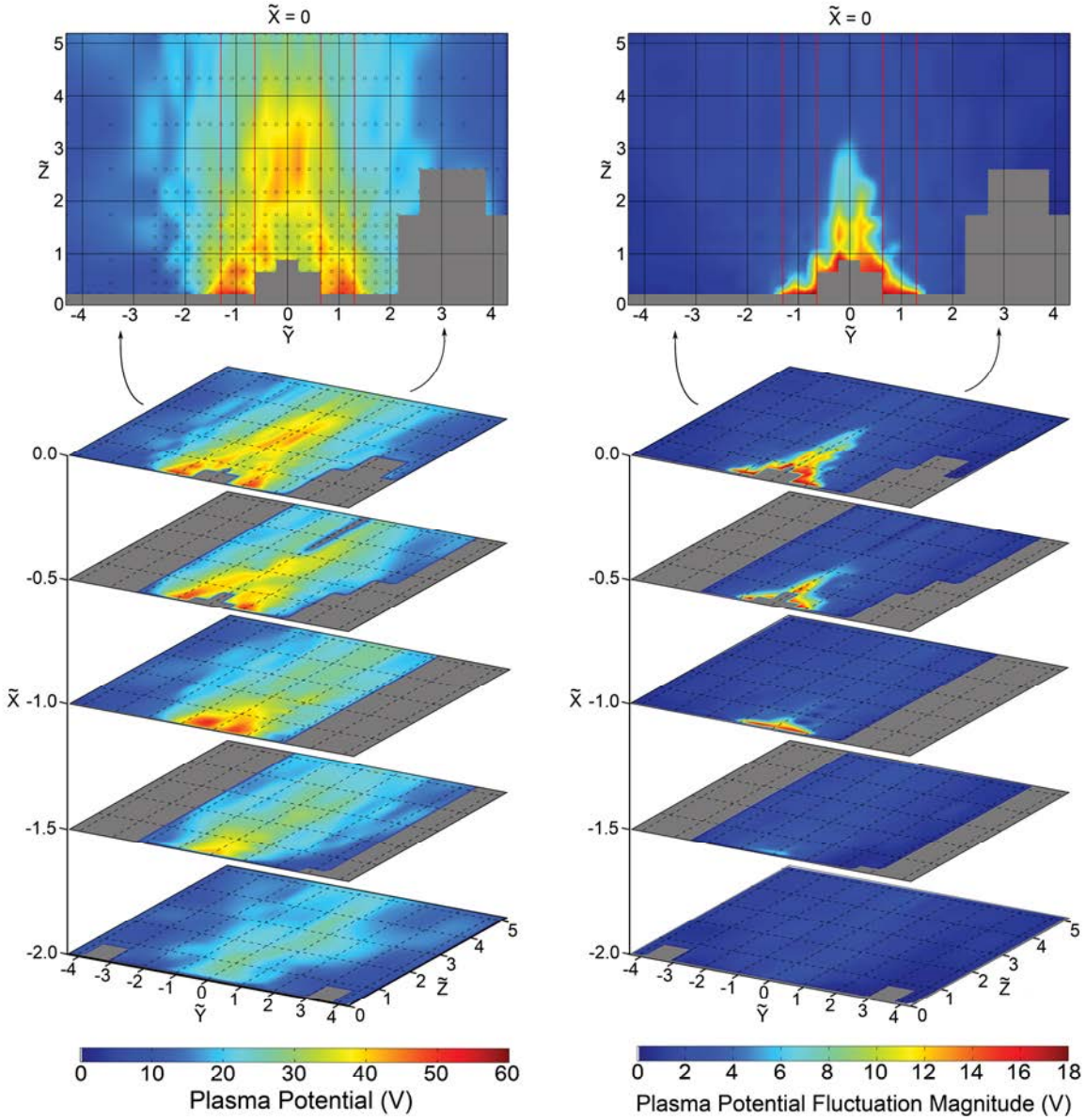

Figure 6. Spatial slices of the measured plasma potential (left) and magnitude of the plasma potential fluctuations (right).

elevated electron temperature extend out to and beyond $z = 4\ r_m$. This central region of elevated electron temperature is separated by a narrow and shallow valley of lower temperature, similar in form to the plasma potential. A strong depression in the electron temperature exists along the central axis for $z < \sim 2\ r_m$, where it reaches a minimum of 3 eV. This depression is surrounded by nearly continuous ridges of elevated electron temperature (> 7 eV) which link the near-channel regions to the high-temperature spike along the axis at $z > \sim 2\ r_m$. Elsewhere, the electron temperature diminishes to < ~5 V, and becomes somewhat more uniform.

The electron temperature fluctuations are largest (> 4 eV) in the regions nearest the channel exit, as shown in the right panel of Fig. 7. As was noted previously for the plasma and floating potential, the fluctuation magnitude is greatest where the mean electron temperature is highest; however, in the region of $z > 2\ r_m$ along the central axis, the electron temperature shows significantly smaller fluctuations than would be expected from this correlation. The fluctuations rapidly diminish for x, y, or $z > 1\ r_m$ (except along the central axis).

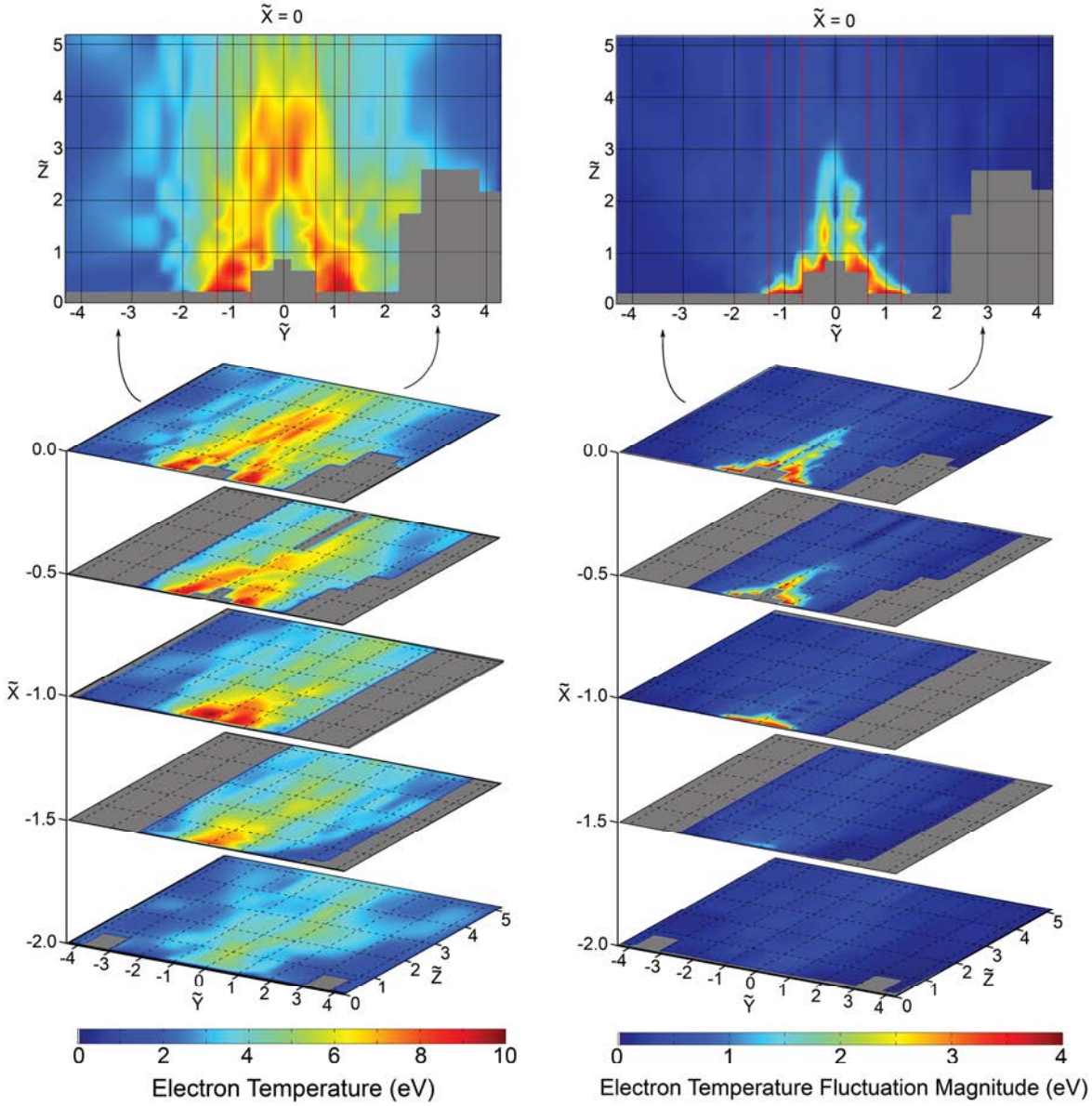

Figure 7. Spatial slices of the inferred electron temperature (left) and magnitude of the electron temperature fluctuations (right).

B. Time-correlated Results

The discharge current and probe signals are measured simultaneously, allowing us to reconstruct the time-correlated properties throughout the near-field by synchronizing the temporal data to dominant low-frequency discharge current fluctuations, which are often attributed to the breathing mode[21]. This approach is the same as that taken by Albarede et al[17] in their investigation of low-frequency electron dynamics in the near-field of a Hall thruster. The frequency of this breathing mode oscillation is expected to be governed by the residence time of neutral atoms in the acceleration region of the thruster. A reasonable estimate of the neutral xenon velocity is ~ 1.7×10^4 cm/s, i.e., about the sonic velocity at room temperature. The acceleration zone is estimated to be around 0.5-1.0 cm long, so we expect the breathing mode frequency to be on the order of 20-30 kHz, a value confirmed by measurements made on a similar thruster by Hargus and Pote[29].

In post-processing the data, we survey the discharge current traces at each spatial location, and take the first breathing-mode peak in the discharge current to be $t = 0$ (i.e. the initial time) for the probe data at this spatial point (see Fig. 4). We repeat this process for all of the measurement locations, yielding "synchronized" measurements based on an initial peak in the breathing mode. This method does not yield an absolute determination of the temporal field structure for two primary reasons: first, the measurements were all recorded at separate moments in time, and although the thruster was in steady-state operation, the discharge properties are not identical from one breathing mode to the next. However, the variability in the mean discharge current was small, and the consistency of neighboring measurements (which were not recorded sequentially due to the motion algorithm used to scan the measurement volume) reinforces the validity of our method. Second, the determination of a breathing mode peak is not absolute given the many higher-frequency oscillations present in the signals (see Fig. 4). We estimate that the zero datum ($t = 0$) may vary by as much as 5-10 μs due to the higher-frequency oscillations which blur the breathing mode oscillations. This error is non-systematic (sometimes causing an early start point and sometimes a late start point), however, and we expect that these errors may cancel when viewed over many points.

Figures 8 and 10 show the measured plasma properties in the $x = 0$ plane at representative time synchronizations encompassing a range of 40 μs with 5 μs intervals and Fig. 9 shows the plasma potential in the $z = 0.4\ r_m$ plane at six representative times spanning 25 μs. This range of time was chosen because it is approximately the duration of one breathing mode oscillation, and the primary fluctuations present in the near field appear to oscillate at this rate. Figures 8, 9, and 10 are also synchronized to each other, with $t = 0$ the same for each figure. This allows for visualization of the simultaneous variation of the floating potential, plasma potential, and electron temperature.

The temporal fluctuation in floating potential (see Fig. 8, left pane) is less strong than the fluctuation in the plasma potential and electron temperature. The most visible feature is an axial oscillation of the elevated potential region along the central axis. In the figure, the image at $t = 0$ shows two regions of elevated potential along the central axis; the first at $0.75\ r_m < z < 1.5\ r_m$, and the second at $2.0\ r_m < z < 2.5\ r_m$. The peak potential in both of these regions is ~13 V with the intermediate region dropping to around 10 V. In subsequent snapshots, the potential in both regions increases and the features merge into a single axially-elongated region of elevated potential spanning $0.75\ r_m < z < 2\ r_m$. The process repeats at a rate on the order of the breathing mode frequency (~25 kHz). Other oscillations are present, most notably a subtle bulk oscillation in the magnitude of the floating potential throughout the near-field.

The plasma potential exhibits a highly complex, dynamic transient behavior as shown in the right pane of Fig. 8. At first glance, the plasma potential appears somewhat turbulent; however, a closer inspection reveals subtle patterns in the fluctuations. The most dramatic transient feature is an apparent azimuthal rotation of the regions of elevated plasma potential about the central axis (better shown in Fig. 9). In the first image at $t = 0$, there is a broad region of high potential (exceeding 55 V) extending over the central portion of the thruster both over the channels and near the central axis for $z < 1\ r_m$. The central peak in potential along the axis is not split (as the time-averaged results indicated); rather it there exists a single peak shifted away from the axis towards positive values of y. Later, at $t = 15$ μs, the maximum potential decreases to 45 V, and the region of elevated potential near the axis has started to separate from the regions over the channels and is more strongly shifted toward positive values of y. At $t = 20$ μs and 25 μs, the plasma potential located over the portion of the channel centered at $y = r_m$ is intensifying while the potential over the opposing portion of the channel (centered at $y = -r_m$) is diminishing. The plasma potential along the central axis for $z < 2\ r_m$ starts falling at this time, dropping below 20 V. At the same time, the downstream peak in potential increases in magnitude for $y > 0$. In the final frames, the elevated plasma potential over the channel centered at $y = -r_m$ returns. This sequence of events repeats over time with a frequency close to the breathing mode.

Further details into the character of the fluctuations can be obtained by examining the results in a spatial plane parallel to the exit plane. Figure 9 shows the plasma potential in the $z = 0.4\ r_m$ plane (i.e. just beyond the exit plane) with the channel boundaries indicated with black semicircles (measurements were only obtained for $x > 0$). In this series of images, a region of elevated plasma potential rotates azimuthally in a counter-clockwise direction which is opposite the general $\boldsymbol{E} \times \boldsymbol{B}$ direction, consistent perhaps with density-gradient driven drift waves. This fluctuation appears to be a single wave which rotates about the channel with a wavenumber of approximately 14 $m^{-1}$and repeats at ~25 kHz, indicating an azimuthal velocity of approximately 1800 m/s. The velocity is approximately four times the azimuthal velocity reported by Hargus et al[30] and seven times the value reported by Manzella et al[31] which is not surprising considering that different thrusters are involved and that, while our measurements track the plasma potential, those of Refs. 30-31 are tracking the ions themselves.

The electron temperature (see Fig. 10) shows the same qualitative dynamical behavior as the plasma potential (as expected, since the floating potential was found to be fairly quiescent). However, the effect of the axially-oscillating floating potential spike along the centerline manifests itself as an oscillation in the electron temperature along the central axis (fluctuating from ~1 eV up to ~7 eV at $z = r_m$). At $t = 0$, there is a broad region of elevated

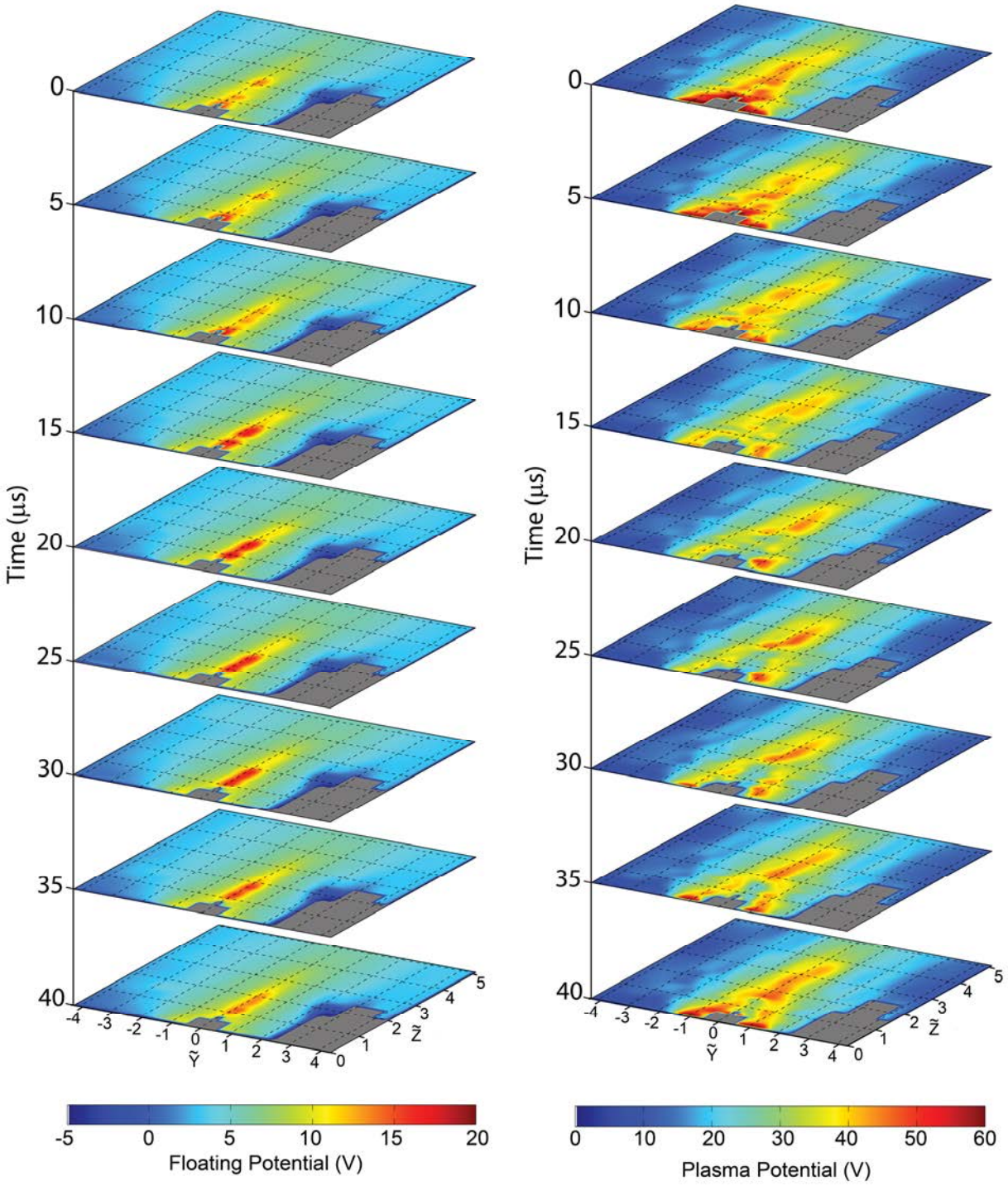

Figure 8. Temporal snapshots of the floating potential (left) and plasma potential (right) in the $x = 0$ plane.

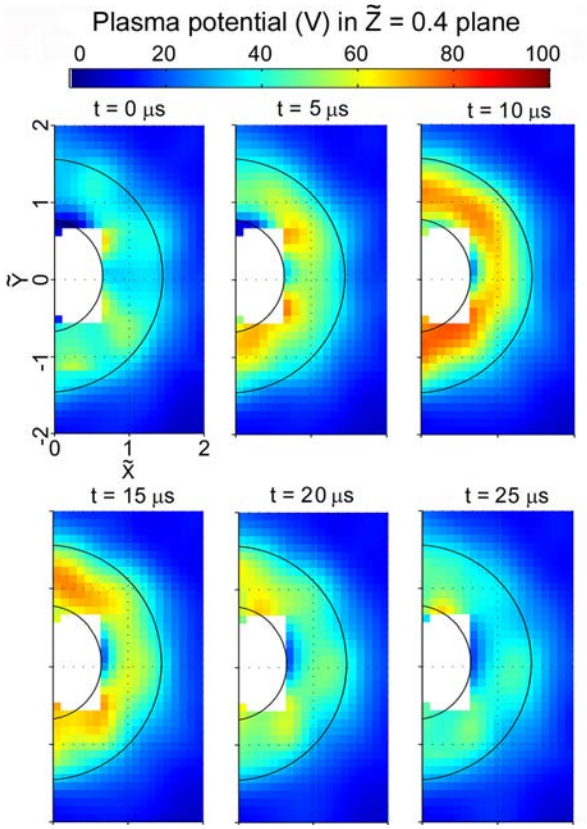

Figure 9. Temporal snapshots of the plasma potential in the $z = 0.4\ r_m$ plane.

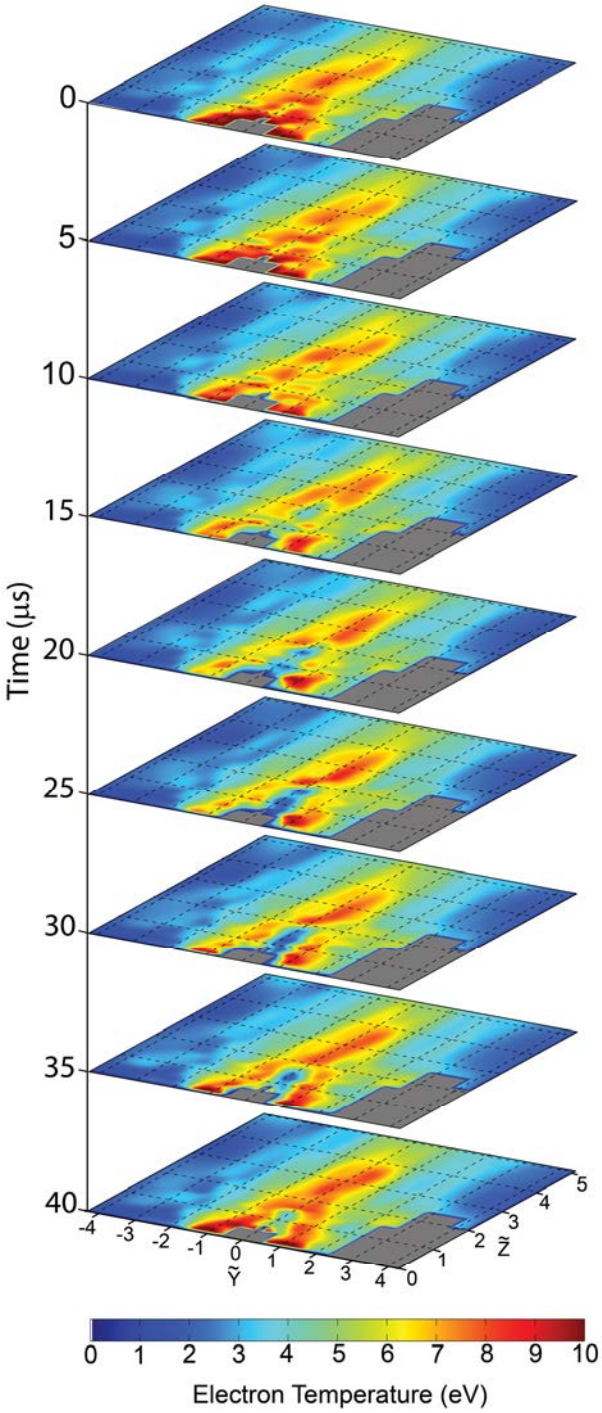

Figure 10. Temporal snapshots of the inferred electron temperature in the $x = 0$ plane.

electron temperature extending between $-2\ r_m < y < 2\ r_m$ and $z < 5\ r_m$ which is, for the most part, continuous with small regions of locally-reduced electron temperature. One of the most notable regions of low electron temperature occurs near the central pole of the thruster (i.e. near $y = 0$ for $z < 1.5\ r_m$). In subsequent frames, the continuous region of elevated electron temperature begins to break apart, and a significant depression in the electron temperature forms along the central axis near the thruster for $z < 2\ r_m$. A sharp discontinuity in electron temperature develops near $z = 2\ r_m$ for times between $t =$ 15 μs and $t = 35$ μs. The electron temperature in this depression decreases to values less than 1 eV before the depression starts to merge with the surrounding elevated electron temperature regions. The regions of elevated electron temperature mimic the temporal behavior of the plasma potential and oscillate in a twisting (helical) motion about the central axis of the thruster.

IV. Discussion and Summary

We have carried out an extensive survey of the floating potential, plasma potential, and electron temperature throughout the near-field of a coaxial Hall plasma accelerator and found these properties to be highly structured, and, in the case of the plasma potential and electron temperature, highly variable in time. The time-averaged floating potential shows a strongly-elevated beam-like region (with a peak of 18 V) along the central axis of the thruster extending more than two mean channel radii away from the exit plane. The central spike is tightly bound to the

central axis, diminishing completely within 1 r_m in the x- and y-directions while extending to $z = 3\ r_m$. The presence of the cathode manifests itself as a deep depression in the potential (< -5 V). On the whole, the overall floating potential distribution is quite axisymmetric.

The plasma potential exhibits considerably more structure with regions of elevated potential over the channels (where the potential exceeds 55 V) and steep, broad ridges of elevated potential connecting to a central split peak along the centerline for $z > \sim 1.6\ r_m$. The potential along the centerline remains elevated to nearly 4 r_m from the exit plane. A deep depression in the plasma potential exists along the central axis near the exit plane for $z <\sim 2\ r_m$ in which the plasma potential falls to ~30 V (surrounded by regions where the plasma potential reaches 40 to 45 V). This structure allows for the acceleration of back-streaming ions toward the thruster; these ions may be responsible for some of the lifetime-limiting erosion of the insulator materials near the exit plane, and in particular on the central pole of Hall thrusters. If a low-energy ion is present along the central axis near $z \sim 2\ r_m$ (perhaps created via a charge-exchange collision), it will be accelerated towards the thruster. Furthermore, low-energy ions exiting the thruster close to the inner edge of the channel will be drawn towards the central axis.

The electron temperature is elevated over the channel and along the central axis, with ridges connecting the two regions, and it exhibits a strong depression along the axis for $z < \sim 2\ r_m$ where the temperature falls to 3 eV. Bordering this depression, steep gradients in the electron temperature (in the $\pm x$-, $\pm y$-, and $+z$-direction) lead to surrounding regions in which the electron temperature exceeds 7-8 eV.

The results illustrate that the transient plasma potential structure is complex with many fluctuations occurring throughout the near-field. The dominant fluctuation in the floating potential is an axial oscillation along the central axis in which two separated regions of elevated potential converge and combine before subsequently splitting and rebounding. The dominant fluctuation in the plasma potential is an azimuthal oscillation over the channel and along the central axis. In addition to this azimuthal oscillation, we find many elevated regions of plasma potential which connect the channel region to the broad spike in plasma potential located along the central axis and oscillate back and forth. The electron temperature generally follows the plasma potential in terms of the fluctuation structure, however, there is an additional oscillation along the central axis for $z <\sim 2\ r_m$ where the electron temperature oscillates between very low and more moderate values.

Both the electron temperature and plasma potential are expected to be underestimated (see Section 2). Given the range of electron temperature measured, the plasma potential is expected to be underestimated by as much as 15 V near the exit plane, and 4 V at the outer extend of the experiment domain.

All three of the plasma properties show a distinct transition along the axis near $z = 2\ r_m$. In the floating potential, the prominent spike in potential along the axis sharply diminishes for $z > 2\ r_m$. A broad depression in the plasma potential extends along the central axis up to $z \sim 2\ r_m$, at which point the plasma potential quickly rises to > 45V. This transition is manifested most clearly in the electron temperature which, at some instants in time, rises from a low along the axis of <1 eV at $z \sim 1.9\ r_m$ to > 8eV at $z \sim 2\ r_m$ (see Fig. 10, t = 25, 30 μs). To our knowledge, there is no explanation for the location of this transition in the literature, and this feature will be the studied further in future research.

The nature of the apparent structure of the plasma potential and electron temperature fluctuations is well explained if a twisting, helical disturbance is present in the near-field potential. This twisting mode may be due to coupling of the breathing mode oscillation[21] and low-frequency azimuthal ($\boldsymbol{E} \times \boldsymbol{B}$) oscillations[4] related to either the ionization process or to density gradient-driven drift wave instabilities[21]. In an early study, Janes and Lowder[4] found that the observed electron diffusion across magnetic field lines is much greater than collisional diffusion processes could account for, and they attributed this "anomalous" diffusion to the transport resulting from low frequency azimuthal waves.

The significant fluctuations measured in the near-field lend support to the possible role that fluctuations may play in the anomalous cross-field diffusion of electrons from the external cathode to the exit plane of the thruster. We have estimated the cross-field transport that might occur from these relatively low frequency disturbances within the framework of a drift-resistive instability driven by axial density gradients of characteristic scale, $L_{\nabla_n} \approx O\left(10^{-2}\right)$m. Following Ref. 32, the dispersion of these waves is approximately:

$$\omega \approx \omega_e^* \left(1 + i\alpha/4\right)\left(1 + k_\perp^2 \rho_s^2\right)^{-1}, \tag{2}$$

where $\omega_e^* = \frac{k_\theta k T_e}{eBL_{\nabla_n}} \approx$ 4x10^6 rad/s is the characteristic drift-wave frequency, with $k_\theta \approx 50$ rad/m and $k_z = \left(k_\perp^2 - k_\theta^2\right)^{1/2} \approx 50$ rad/m, the azimuthal and axial component wavenumbers (waves appear to propagate at about 45^o, forming the helix), and $\rho_s = c_i/\omega_{ci} \approx 0.15$ m, i.e., the ratio of the ion acoustic speed to the ion cyclotron frequency. The parameter α ($\approx$ 4x10^{-3} in this case) is proportional to the growth rate of the drift wave instability,

$$\alpha \approx 4\omega_e^* / \omega_s \left(1 + k_\perp^2 \rho_s^2\right)^2, \tag{3}$$

where $\omega_s \approx \omega_{ce}\omega_{ci}/\nu_e$ ($\approx$7 x 10^5 rad/s in our case) the product of the electron and ion cyclotron frequencies, and the inverse electron collision frequency, taken to be the bounce frequency between the inner and outer magnetic pole ($\approx$ 10^7 s^{-1}).

A quasilinear estimate can be made of the axial electron current in the near field, from the measured fluctuation amplitudes in plasma potential, $\tilde{\phi} \approx$ 10 V. From the predicted fluctuation amplitudes in both plasma density and electron velocity, we estimate:

$$J_e \approx \frac{\alpha n_o e^2 k_\theta k_\perp^2 \rho_s^2}{4kT_e B}\tilde{\phi}^2 \approx 10^2 A/m^2 \cdot \tag{4}$$

With an exit plane area of approximately 10^{-3} m^2, this corresponds to a current of about 0.1 A, or roughly 10% of the discharge current. At this value, these low frequency drift waves may account for some portion of the anode-directed electron current density in the very near field of these Hall discharges, however, we note that the frequency predicted by the dispersion equation above is about a factor of 3-4 lower than that seen in the experiments, and that the theory presented in Ref. 32 is for a non-current carrying plasma. The theory requires refinement to account for the relatively large current carried axially in the base (unperturbed plasma) and is the subject of future work.

Acknowledgments

This research was supported by the Air Force Office of Scientific Research, with Dr. Mitat Birkan as program manager. A. W. Smith acknowledges support through the National Defense Science and Engineering Graduate Fellowship program.

References

[1]Grossman, W., Hess, R. V., and Hassan, H. A., "Experiments with a coaxial Hall current plasma accelerator," *AIAA Journal*, Vol. 6, 1965, pp. 1034

[2]Morozov, A. I., Kislov, A. Y., and Zubkov, I. P., "Strong-current plasma accelerator with closed electron-drift," *JETP Letters,* Vol.. 7, 1968, pp. 172

[3]Hargus, W. A., and Cappelli, M. A., "Laser-induced fluorescence measurements of velocity within a Hall discharge" *Applied Physics B*, Vol. 72, 2001, pp. 961-969

[4]Janes, G. S., and Lowder, R. S., "Anomalous electron diffusion and ion acceleration in a low-density plasma," *Physics of Fluids*, Vol. 9, 1966, pp. 1115-1123

[5]Meezan, N. B., Hargus, W. A., and Cappelli, M. A., "Anomalous electron mobility in a coaxial Hall discharge plasma," *Physical Review E*, Vol. 63, 2001, 026410

[6]Lazurenko, A., de Wit, T. D., Cavoit, C., Krasnoselskikh, V., Bouchoule, A., and Dudeck, M., "Determination of the electron anomalous mobility through measurements of turbulent magnetic field in Hall thrusters," *Physics of Plasmas*, Vol. 14, 2007, 033504

[7]Bohm, D., Burhop, H. S., and Massey, H. S. W., *"The characteristics of electrical discharges in magnetic fields*," Eds. Guthrie, A., Wakerling, R. K., McGraw Hill, New York, 1949.

[8]Morozov, A. I., and Savel'ev, V. V., "Theory of the near-wall conductivity," *Plasma Physics Reports*, Vol. 27, 2001, pp. 570-575

[9]Barral, S., Makowski, K., Peradzynski, Z., Gascon, N., and Dudeck, M., "Wall material effects in stationary plasma thrusters. II. Near-wall and in-wall conductivity," *Physics of Plasmas*, Vol. 10, 2003, pp. 4137-4152

[10]Fife, J. M. "Hybrid-PIC Modeling and electrostatic probe survey of Hall thrusters", Ph.D. Dissertation, Aeronautics and Astronautics Dept., Massachusetts Institute of Technology, Cambridge, MA, 1998

[11]Hagelaar, G. J. M., Bareilles, J., Garrigues, L., and Boeuf, J. P., "Two-dimensional model of a stationary plasma thruster," *Journal of Applied Phys*ics*,* Vol. 91, 2002, pp. 5592-5598

[12]Beal, B. E., Gallimore, A. D., and Hargus, W. A., "Plasma properties downstream of a low-power Hall thruster," *Physics of Plasmas*, Vol. 12, 2005, 123503

[13]Beal, B. E., Gallimore, A. D., Haas, J. M., and Hargus, W. A., "Plasma properties in the plume of a Hall thruster cluster," *Journal of Propulsion and Power*, Vol. 20, 2004, pp. 985-991

[14]Hargus, W. A., and Cappelli, M. A., "Interior and exterior laser-induced fluorescence and plasma measurements within a Hall thruster," *Journal of Propulsion and Power*, Vol. 18, 2002, pp. 159-168

[15]Smirnov, A., Raitses, Y., and Fisch, N. J., "Plasma measurements in a 100W cylindrical Hall thruster," *Journal of Applied Physics* Vol. 95, 2004, pp. 2283-2292

[16]Shirasaki, A., and Tahara, H., "Operational characteristics and plasma measurements in cylindrical Hall thrusters," *Journal of Applied Physics*, Vol. 101, 2007, 073307

[17]Albarede, L., Mazouffre, S., Bouchoule, A., and Dudeck, M., "Low-frequency electron dynamics in the near field of a Hall effect thruster," *Physics of Plasmas*, Vol. 13, 2006, 063505

[18]Smith, A, W., and Cappelli, M. A., "Time and Space-correlated plasma potential measurements in the near field of a coaxial Hall plasma discharge," *Physics of Plasmas*, Vol. 16, 2009, 073504

[19]Hruby, V., Monheiser, J., Pote, B., Rostler, P., Kolencik, J., and Freeman, C. "Development of low power Hall thrusters," *30th Plasma Dynamics and Lasers Conference*, 1999, AIAA Paper 1999-3534

[20]Boeuf, J. P., and Garrigues, L. "Low frequency oscillations in a stationary plasma thruster," *Journal of Applied Physics*, Vol. 84, 1998, pp. 3541-3554

[21]Choueiri, E. Y., "Plasma oscillations in Hall thrusters," *Physics of Plasmas*, Vol. 8, 2000, pp. 1411-1426

[22]Haas, J. M., and Gallimore, A. D., "Internal plasma potential profiles in a laboratory-model Hall thruster," *Physics of Plasmas*, Vol. 8, 2001, pp. 652-660

[23]N. Hershkowitz, "*Plasma Diagnostics, Vol. 1 Discharge Parameters and Chemistry*," Eds. by O. Auciello and D.L. Flamm, Academic Press, New York, 1989.

[24]Hargus, W. A., "Investigation of the plasma acceleration mechanism within a coaxial Hall thruster," Ph.D. Thesis, Mechanical Engineering Department, Stanford University, 2001.

[25]Kemp, R. F., and Sellen, J. M., "Plasma potential measurements by electron emissive probes," *Review of Scientific Instruments*, Vol. 37, 1966, 455-461

[26]Navrotskii, A., "Blacksmithing – Basic information on metal," *Metallurgist*, Vol. 25, 1991, pp. 126-129

[27]Dorf, L. Raitses, Y., Fisch, N. J., "Electrostatic probe apparatus for measurements in the near-anode region of Hall thrusters," *Review of Scientific Instruments*, Vol. 75, 2004, pp. 1255-1260

[28]Raitses, Y., Staack, D., Smirnov, A., and Fisch, N. J. "Space charge saturated sheath regime and electron temperature saturation in Hall thrusters," *Physics of Plasmas*, Vol. 12, 2005, 073507

[29]Hargus, W. A., and Pote, B., "Examination of Hall thruster start variant", *38th AIAA/ASME/SAE/ASEE Joint Propulsion Conference*, 2002, AIAA-2002-3956.

[30]Hargus, W. A., and Charles, C. S., "Near plume laser induced fluorescence velocity measurements of a 600 W Hall thruster," *44th AIAA/ASME/SME/SAE/ASEE Joint Propulsion Conference*, Hartford, CT, 2008, AIAA Paper: 2008-5004-404.

[31]Manzella, D. H., "Stationary plasma thruster ion velocity distribution," *30th AIAA/ASME/SME/SAE/ASEE Joint Propulsion Conference*, Indianapolis, IN, 1994, AIAA Paper: 1994-3141.

[32]Swanson, D. G., "*Plasma Waves (2nd Edition)*", Eds. Cowley, S., Stott, P., and Wilhemsson, H., Institute of Physics Publishing, Philadelphia, PA, 2003, pp. 308-310.